ACS Energy LETTERS

Cite This: *ACS Energy Lett.* 2019, 4, 456−463

http://pubs.acs.org/journal/aelccp

Origin of Low Carrier Mobilities in Halide Perovskites

Samuel Poncé,[†] Martin Schlipf,[†] and Feliciano Giustino*,[†,‡]

[†]Department of Materials, University of Oxford, Parks Road, Oxford OX1 3PH, United Kingdom

[‡]Department of Materials Science and Engineering, Cornell University, Ithaca, New York 14853, United States

Supporting Information

ABSTRACT: Halide perovskites constitute a new class of semiconductors that hold promise for low-cost solar cells and optoelectronics. One key property of these materials is the electron mobility, which determines the average electron speed due to a driving electric field. Here we elucidate the atomic-scale mechanisms and theoretical limits of carrier mobilities in halide perovskites by performing a comparative analysis of the archetypal compound $CH_3NH_3PbI_3$, its inorganic counterpart $CsPbI_3$, and a classic semiconductor for light-emitting diodes, wurtzite GaN, using cutting-edge many-body ab initio calculations. We demonstrate that low-energy longitudinal-optical phonons associated with fluctuations of the Pb−I bonds ultimately limit the mobility to 80 cm^2/(V s) at room temperature. By extending our analysis to a broad class of compounds, we identify a universal scaling law for the carrier mobility in halide perovskites, and we establish the design principles to realize high-mobility materials.

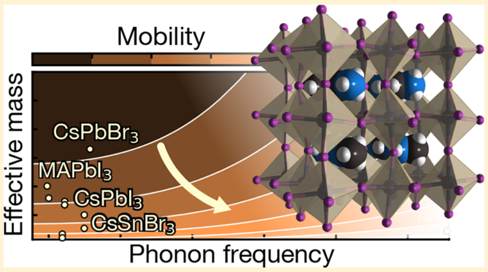

The discovery of halide perovskites has ushered in a new era in photovoltaics and optoelectronics research.[1,2] Originally introduced as active layers for solar cells,[3−5] organic−inorganic lead-halide perovskites and related compounds have shown great promise for a diverse array of applications, including photodetectors, light-emitting diodes (LEDs), semiconductor lasers, optical refrigerators, X-ray and gamma-ray detectors, photocatalysts, thermochromic windows, metal-halide perovskite transitors, and thin-film field-effect transistors.[6−13] The main appeal of these materials is that they can be fabricated via solution processes, yet they exhibit outstanding optoelectronic properties, to the point that they have been designated as the "first high-quality halide semiconductors".[14] In all these devices, the carrier mobility plays a central role. For example, it is a key ingredient of optoelectronic device simulators based on drift-diffusion models. Furthermore, the photoconductive gain in photodetectors and the cutoff frequency in thin-film transistors are directly proportional to the mobility. The cutoff frequency is especially important for realizing gigahertz wireless connectivity.[15]

Further progress in the use of halide perovskites in electronics, optoelectronics, and energy will require us to understand and control the microscopic mechanisms that underpin the optical and transport properties of these materials. While a broad consensus has emerged on their optical properties,[16] understanding carrier transport is proving elusive.[17] For example, measurements of the carrier mobility show striking variations among different laboratories, ranging from 0.07 cm^2/(V s) for room-temperature electron drift mobilities measured in thin films of $CH_3NH_3PbI_3$ prepared via spin-coating[13] to 67 cm^2/(V s) extracted from current−voltage measurements on single-crystals of $CH_3NH_3PbI_3$.[18] Such a large variability in the reported carrier mobilities has been ascribed to differences in sample morphology (single crystals vs films), preparation routes (solid state vs solution or evaporation), and measurement techniques (e.g., Hall effect, time-of-flight, THz conductivity, and photoluminescence quenching).[17] In the face of this high level of uncertainty in the measurements, it is important to identify the ultimate theoretically achievable carrier mobility, and which materials parameters control this limit, so as to set out clear guidelines for materials and device engineering.

In this work we turn to quantum-mechanical calculations in order to establish the ultimate mobility of the archetypal organic−inorganic perovskite, methylammonium lead triiodide $CH_3NH_3PbI_3$ ($MAPbI_3$). There have been several attempts in this direction, but because earlier calculations relied on empirical scattering rates[19,20] or deformation potentials,[21,22] these estimates carry the very same uncertainties that we seek to eliminate. At variance with earlier work, we employ a recently developed ab initio many-body computational technique that enables predictive, parameter-free, and accurate calculations of mobilities, with deviations from the measurements as little as a few percent.[23] This new tool allows us to establish which atomic-scale mechanism dominates the

Received: December 2, 2018
Accepted: January 11, 2019

DOI: 10.1021/acsenergylett.8b02346
ACS Energy Lett. 2019, 4, 456−463

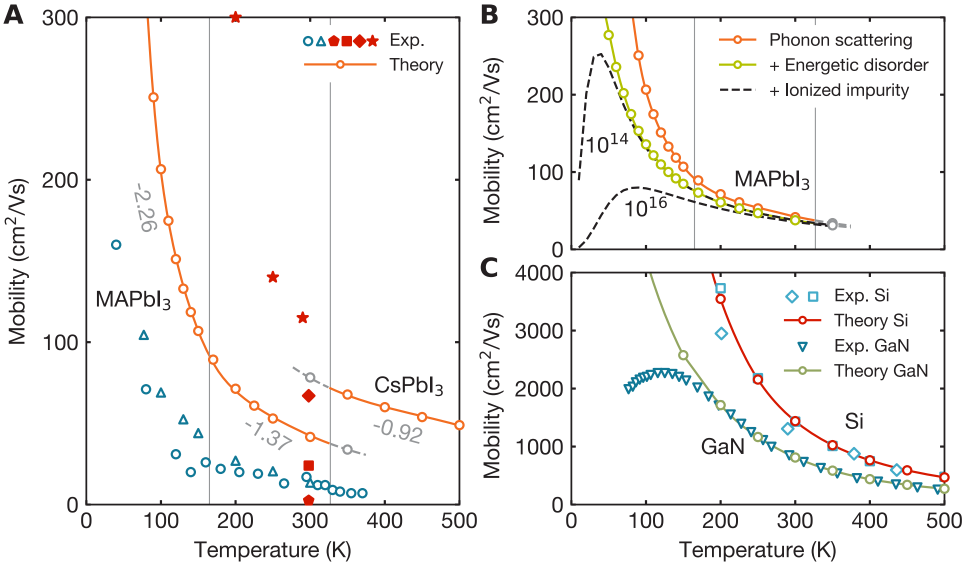

Figure 1. Temperature-dependent carrier mobilities in MAPbI$_3$, CsPbI$_3$, and GaN. (A) Average electron and hole phonon-limited mobilities calculated from the ab initio many-body Boltzmann equation for MAPbI$_3$ in the *Pnma* structure (circles and solid orange lines between 0 and 350 K) and CsPbI$_3$ in the *Pm*$\bar{3}$*m* structure, at the lattice parameter of MAPbI$_3$, between 250 and 500 K. The experimental data are from ref 24 (circles, optical pump−THz probe) and ref 25 (triangles, ultrabroadband THz photoconductivity) taken on thin films, whereas the filled red symbols are taken on single crystals in ref 26 (pentagon, space-charge-limited current), ref 27 (square, time-of-flight), ref 18 (diamond, dark current−voltage), and ref 28 (star, time-of-flight). All calculations were performed without any artificial broadening and therefore represent theoretical upper bounds. The vertical bars indicate the boundaries of the orthorhombic, tetragonal, and cubic phases of MAPbI$_3$, while the gray numbers indicate the exponent for the temperature dependence of the three phases. (B) Impact of energetic disorder and ionized impurity scattering on the ideal mobility of MAPbI$_3$: we compare the average of the phonon-limited electron and hole mobilities from panel A (orange line) with that obtained after including a 13 meV broadening of the electronic states (from the Urbach tail measured in ref 29) (green line) and scattering by ionized impurities at the concentrations 10^{14} and 10^{16} cm^{-3}, from ref 30 (black dashed lines). The impurity scattering is calculated using the semiempirical Brook−Herring model.(C) Electron mobility of GaN as a function of temperature: present calculations (green circles and line) versus mobilities extracted from Hall effect measurements in ref 31 (triangles). The theoretical electron mobility of silicon is from ref 23 (red circles and line), and the experiments (diamonds and squares) are from ref 32.

mobility in halide perovskites and answer the question why the mobility of MAPbI$_3$ is orders of magnitude lower than in inorganic semiconductors such as GaN. Using this understanding we propose strategies to overcome the mobility bottleneck and illustrate the practical benefits of realizing high-mobility perovskites.

Figure 1A shows the phonon-limited mobility of MAPbI$_3$ calculated for a perfect, defect-free bulk crystal in the low-temperature orthorhombic *Pnma* structure. In this structure, the MA$^+$ cations (methylammonium, CH$_3$NH$_3$$^+$) have definite crystallographic orientations, as shown in the ball−stick model of Figure 2A. This model is accurate for the orthorhombic phase of MAPbI$_3$ (T = 0−165 K) and provides a good approximation to the tetragonal *I*4/*mcm* phase (T = 165−327 K), where the MA$^+$ cation spins around the C−N axis and aligns along one of four preferred orientations in the *ab* plane.[33−35] For the high-temperature *Pm*$\bar{3}$*m* cubic phase (T > 327 K), neutron scattering indicates that the organic cations are rotationally disordered,[36] with preferential orientation along the [111], [100], and [011] directions. In order to mimick orientational disorder, we perform calculations for cubic CsPbI$_3$ at the lattice parameter of MAPbI$_3$, as shown by the ball−stick model in Figure 2B. The corresponding mobilities are reported in Figure 1A in the temperature range above 327 K.

In Figure 1A we see that the calculated electron and hole mobilities decrease with temperature, from ~500 cm^2/(V s) below 100 K to 28 and 47 cm^2/(V s) at room temperature for electrons and holes, respectively. These values constitute theoretical upper bounds, because at this stage we are considering only electron−phonon scattering in the undoped, defect-free crystal. Because our data correspond to intrinsic mobilities in bulk perovskites, the most appropriate way to compare with experiments is to consider corrected Hall measurements, time-of-flight, or steady-state photoconductivity measurements[28,37,38] on MAPbI$_3$ (red symbols in Figure 1A). To extend the comparison throughout the entire temperature range, we also consider transient terahertz (THz) data on thin films. When compared to THz photoconductivity data on thin films[24,25] we see that our calculations yield higher values, as expected, but a similar temperature dependence. In fact, by fitting the calculated data in the temperature ranges corresponding to the orthorhombic, tetragonal, and cubic phases using a power law (aT^b), we find that the mobility scales as $\mu \sim T^{-2.26}$, $\mu \sim T^{-1.37}$, and $\mu \sim T^{-0.92}$, respectively. The exponents determined here broadly agree with previous theoretical work based on analytical models.[20,39,40] In addition, our calculated temperature exponent in the tetragonal phase agrees with the value of −3/2 obtained in the experiments.[24] This power law was previously attributed to acoustic-phonon scattering,[25,37] but as we will discuss below, the dominant scattering mechanism is from polar phonons, in agreement with recent analytical model calculations.[20,41] At the tetragonal-to-cubic transition temperature (327 K), the mobilities of the cubic CsPbI$_3$ phase reach values of 68 and 76 cm^2/(V s) for electrons and holes, respectively. The increase with respect to the orthorhombic MAPbI$_3$ structure is due to stiffer optical phonons and smaller

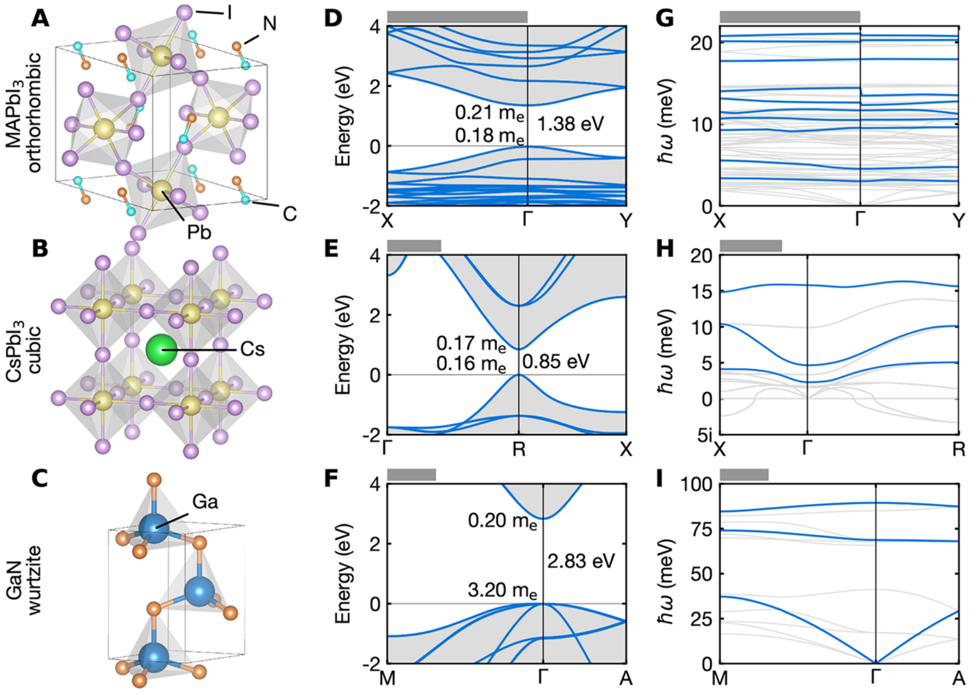

Figure 2. Crystal structure, band structure, and phonon dispersion relations of MAPbI$_3$, CsPbI$_3$, and GaN. Ball−stick models of (A) MAPbI$_3$ in the orthorhombic *Pnma* structure, (B) CsPbI$_3$ in the cubic *Pm*$\bar{3}$*m* structure, and (C) wurtzite GaN. For the MA$^+$ cations, only the C and N atoms are shown for clarity. (D−F) Calculated GW band structures of MAPbI$_3$, CsPbI$_3$, and GaN for the models shown in panels A−C. The valence and conduction bands are shaded for clarity, and the band gaps and effective masses are indicated. (G) Calculated phonon dispersion relations of MAPbI$_3$ for the model in panel A. The lines highlighted in blue represent the LO phonons with strongest electron−phonon coupling. (H) Phonon dispersion relations of CsPbI$_3$, using the same color code as in panel D. The soft modes around the high-symmetry point R = 1/2(1,1,1) (in reciprocal lattice units) do not contribute to the mobility, as shown in Supporting Information, section 1. (I) Phonon dispersion relations of wurtzite GaN. In this case we highlight in blue the LO phonons around 89 meV and the acoustic phonons leading to piezoacoustic scattering. We note that the scales of the horizontal axes in panels D−F and G−I differ; for clarity we indicate in each panel the reciprocal lattice length Γ-X of orthorhombic MAPbI$_3$ as a gray bar.

effective masses, as we show below. In Figure 1B we can see that scattering by charged impurities in MAPbI$_3$ provides a negligible contribution to the mobility at temperatures above 150 K; therefore, in the temperature range relevant for device operation, carrier transport in this system is predominantly phonon-limited.

In order to validate our present calculations we also show in Figure 1C the calculated electron mobilities of prototypical semiconductors for photovoltaics and LEDs: silicon and wurtzite GaN. The latter exhibits an electron effective mass close to that of MAPbI$_3$. Here we see that the agreement with experiments is excellent for temperatures above 150 K.[31] The deviation between our calculations for GaN and experiments at lower temperatures relates to scattering by crystal defects, which we have not included. Overall, this comparison for silicon and gallium nitride demonstrates that our methodology is capable of delivering highly accurate mobilities without using any empirical parameters. On the basis of our calculated values for the orthorhombic and cubic phases in Figure 1A, we predict that the ultimate average electron/hole mobility of MAPbI$_3$ at room temperature lies between 30 and 80 cm^2/(V s). Interestingly, the highest mobility measured on MAPbI$_3$ single crystals, 67 cm^2/(V s),[18] is already approaching this theoretical limit.

We now proceed to a detailed analysis of the mechanisms underpinning the mobilities in Figure 1A. The calculations leading to these data were performed within the framework of the ab initio Boltzmann-transport formalism, using the self-energy relaxation time approximation.[23] The electron mobility tensor reads

$$\mu_{e,\alpha\beta} = -\frac{e}{n_e\Omega}\sum_{n\in \mathrm{CB}}\int\frac{d\mathbf{k}}{\Omega_{\mathrm{BZ}}}\frac{\partial f_{n\mathbf{k}}}{\partial\varepsilon_{n\mathbf{k}}}v_{n\mathbf{k},\alpha}v_{n\mathbf{k},\beta}\tau_{n\mathbf{k}} \tag{1}$$

where e is the electron charge and n_e is the electron density; Ω and Ω_{BZ} are the volume of the crystalline unit cell and the first Brillouin zone, respectively. The sum is restricted to states in the conduction bands (CB) with energy $\varepsilon_{n\mathbf{k}}$, band index n, and wavevector $\mathbf{k}$. $f_{n\mathbf{k}}$ is the Fermi−Dirac function, and $v_{n\mathbf{k},\alpha} = \hbar^{-1}\partial\varepsilon_{n\mathbf{k}}/\partial k_\alpha$ is the electron band velocity along the Cartesian direction α ($\hbar$ is the reduced Planck constant). The relaxation time in eq 1 is given by[42]

$$\frac{1}{\tau_{n\mathbf{k}}} = \frac{2\pi}{\hbar}\sum_{m\nu\sigma}\int\frac{d\mathbf{q}}{\Omega_{\mathrm{BZ}}}|g_{mn\nu}(\mathbf{k},\mathbf{q})|^2[(1+\sigma)/2 - \sigma f_{m\mathbf{k}+\mathbf{q}} + n_{\mathbf{q}\nu}]\delta(\varepsilon_{n\mathbf{k}} - \varepsilon_{m\mathbf{k}+\mathbf{q}} - \sigma\hbar\omega_{\mathbf{q}\nu}) \tag{2}$$

Here $g_{mn\nu}(\mathbf{k},\mathbf{q})$ is the matrix element for the scattering of an electron from the initial state $|n\mathbf{k}\rangle$ to the final state $|m\mathbf{k}+\mathbf{q}\rangle$ via a phonon of branch ν, wavevector $\mathbf{q}$, and frequency $\omega_{\mathbf{q}\nu}$. $n_{\mathbf{q}\nu}$ is the Bose−Einstein occupation of this phonon, and σ takes the values ±1 for phonon emission/absorption, respectively. The temperature enters eqs 1 and 2 via the Fermi−Dirac and Bose−Einstein distributions. The mobility tensor for holes is obtained analogously, by restricting the summation in eq 1 over the valence bands.

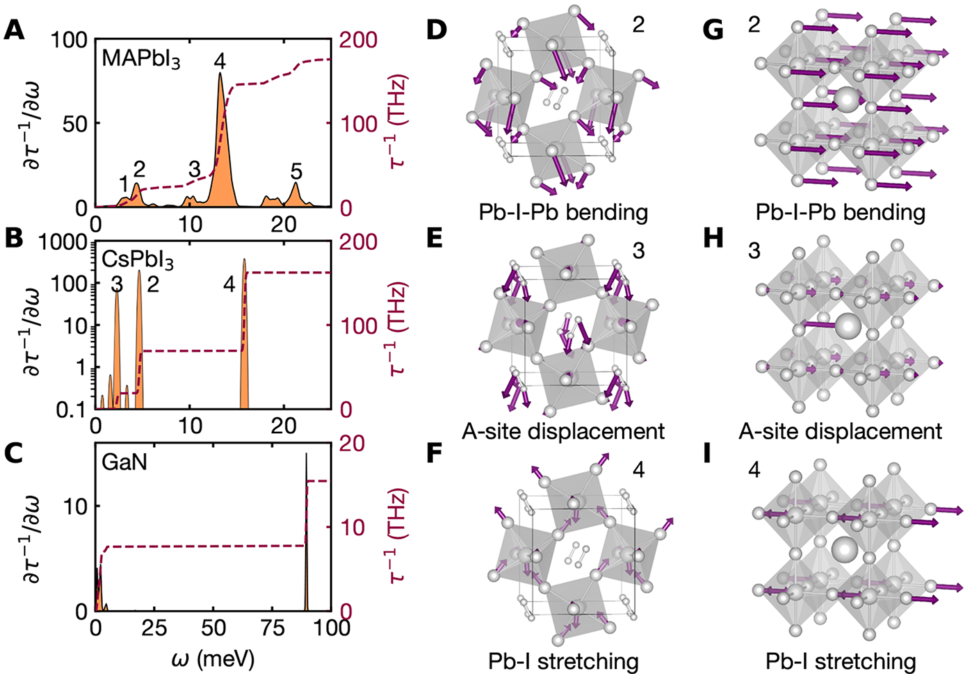

Figure 3. Electron−phonon scattering mechanisms in MAPbI$_3$, CsPbI$_3$, and GaN. (A−C) Spectral decomposition of the contribution of each phonon with energy $\hbar\omega$ to the electron scattering rate $1/\tau_{n\mathbf{k}}$, for MAPbI$_3$ (A), CsPbI$_3$ (B), and GaN (C). The scattering rates are evaluated for electrons at an energy $3/2k_BT$ from the conduction band bottom, with T = 300 K (see the Supporting Information, section 2). The height of the peaks indicates the contribution of each phonon (left vertical axis), and the integral $\int(\partial\tau^{-1}/\partial\omega)\,d\omega$ yields the total scattering rate (right vertical axis). The dashed line indicates the cumulative integral of the differential scattering rate. Acoustic scattering is negligible in MAPbI$_3$ and CsPbI$_3$, while the dominant contributions are from vibrations corresponding to LO phonons, as indicated by the peaks labeled 1−5 described in the main text and illustrated in panels D−F. In the case of GaN, approximately half of the scattering rate arises from piezoacoustic scattering, as shown by the peaks between 0 and 5 meV in panel C. (D−F) Schematic representations of the atomic displacements of MAPbI$_3$ corresponding to the peaks 2−4 identified in panel A. (G−I) Same as in panels D−F but for CsPbI$_3$.

All the quantities entering eqs 1 and 2 are calculated entirely from first principles. In particular, the band structures include state-of-the-art GW quasiparticle corrections to density functional theory with spin−orbit coupling; the phonons are obtained from density functional perturbation theory (DFPT); and the electron−phonon matrix elements are evaluated from DFPT and ab initio Wannier interpolation, as described in the in the Supporting Information, section 4. The scattering of electrons by all phonons, namely acoustic, optical, transverse, and longitudinal modes is included without approximations. To capture both long-range and short-range electron−phonon scattering with the same accuracy, the integrals are evaluated using ultradense Brillouin zone grids.[23] In principle we could go one step beyond eq 1 and evaluate mobilities using the self-consistent Boltzmann equation. However, in systems with cubic symmetry at low fields, this usually leads to a modification of the relaxation-time results by 5−10%;[23] therefore, we do not pursue this direction. In a recent paper,[41] we established using Feynman's model[43] that the electron−phonon coupling in MAPbI$_3$ leads to the formation of large polarons with a radius between 62 and 81 Å, extending over more than 20 PbI$_6$ octahedra. We therefore expect that these polarons should not have a strong effect on the scattering matrix elements and neglect their effect on mobility. Work on the impact of large polarons on the mobility of perovskites is ongoing[40,44−47] but remains an open question.

Figure 2 shows ball−stick models of MAPbI$_3$, CsPbI$_3$, and GaN and compares the respective GW band structures and phonon dispersion relations. MAPbI$_3$ and CsPbI$_3$ exhibit similar effective masses for electrons and holes: m_e^*/m_h^* = 0.18/0.21 m_e vs m_e^*/m_h^*=0.16/0.17 m_e, respectively (m_e is the free electron mass). From these values we obtain a reduced effective mass in MAPbI$_3$ of 0.098m_e, in close agreement with magnetotransport measurements yielding 0.104 ± 0.003 m_e.[48] The band gap of MAPbI$_3$ is also in good agreement with experiments (1.38 eV vs 1.6 eV[16]), the deviation of 0.2 eV being in the typical range of GW calculations (Supporting Information, section 3). In our calculations we do not include temperature renormalization of the band gap because this effect is very small in MAPbI$_3$[16,49] and the effective mass does not change appreciably with temperature.[41] In Figure 2E we see that the band gap of CsPbI$_3$ is considerably narrower than in MAPbI$_3$. This effect relates to the absence of octahedral tilts in the cubic structure, as already discussed in previous work.[50] Moving to GaN, in Figure 2F we see that despite the much wider band gap, the electron effective mass is very similar to MAPbI$_3$ (0.20m_e), therefore it is appropriate to use GaN as a benchmark. Additional data on the effective masses are reported in Table S2 for completeness. From the phonon dispersion relations in Figure 2G−I we see that MAPbI$_3$ exhibits more branches that CsPbI$_3$ and GaN; this is simply related to the larger unit cell (48 atoms per cell as compared to 5 and 4 atoms/cell, respectively). In both MAPbI$_3$ and CsPbI$_3$, the vibrational modes of the PbI$_3$ network extend up to ∼15 meV. The additional branches that can be seen for MAPbI$_3$ in Figure 2G around ∼20 meV are associated with librations of the MA$^+$ cations; these modes do not have a counterpart in CsPbI$_3$. The soft modes that are seen for CsPbI$_3$ in Figure 2H correspond to octahedral tilts and are stabilized by anharmonic effects.[51] Because they have no effect on the carrier mobilities

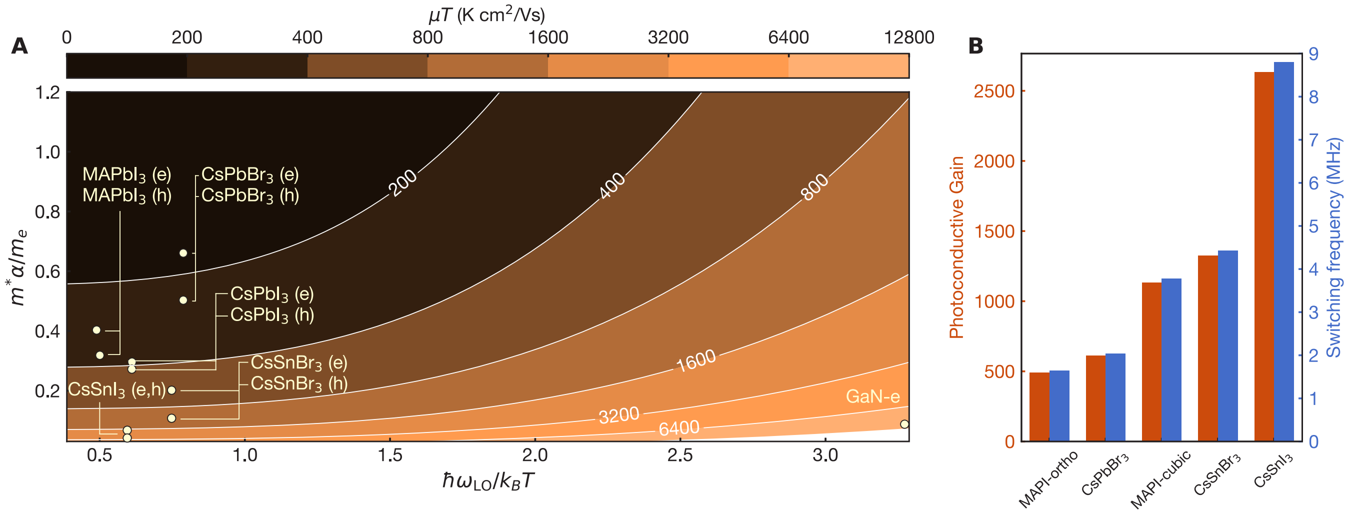

Figure 4. Mobility map of halide perovskites. (A) Calculated carrier mobility within a model including Fröhlich electron−phonon scattering of carriers in a parabolic band. The mobility depends only on the dimensionless parameters $\alpha m^*/m_e$ and $\hbar\omega_{LO}/k_BT$, where α is the Fröhlich coupling strength, m^*/m_e the effective mass relative to the electron mass, and ω_{LO} the frequency of the LO phonon. The details of the model are provided in the Supporting Information, section 2. The predictions of the model for $MAPbI_3$, $CsPbI_3$, $CsPbBr_3$, $CsSnI_3$, $CsSnBr_3$, and GaN are consistent with our complete ab initio calculations, as shown in Table S3. In this table we also report the parameters $\alpha m^*/m_e$ and $\hbar\omega_{LO}/k_BT$ used to locate the various compounds on the map. The horizontal coordinate of each data point corresponds to T = 300 K, and the labels e and h indicate electron and hole mobilities, respectively. The map shows that the key obstacle to achieving high carrier mobilities in halide perovskites is the very low LO phonon energy and that one can circumvent this bottleneck by reducing the polar mass $\alpha m^*/m_e$, as in the case of $CsSnI_3$. (B) Estimated photoconductive gain (red) at 300 K of perovskite photodetectors and switching frequency (blue) of perovskite field-effect transistors, compared to 10^5 and 0.9 THz for GaN, respectively.[55,56] We use $CsPbI_3$ at the lattice parameter of $MAPbI_3$ to approximate the cubic phase of the latter. The evaluation of these performance metrics is discussed in the Supporting Information, section 4.

(Supporting Information, section 1), we do not consider them when evaluating eq 2. In the case of GaN, we see that the highest optical modes reach up to ∼90 meV, as a result of the much lighter masses of Ga and N as compared to Pb and I.

We are now in a position to analyze the origin of carrier mobilities in $MAPbI_3$. Figure 3A−C shows the contribution of each vibrational mode to the total scattering rate $1/\tau_{nk}$ in eq 2. The calculation of mobility in eq 1 requires integration over many electronic states; however, for the present analysis we can focus on the most representative scattering rate (Supporting Information, section 2), which corresponds to states at an energy $3/2k_BT$ from the band edge, with T = 300 K (k_B is the Boltzmann constant). Let us start from GaN and work our way back to $MAPbI_3$. In Figure 3C we see that in GaN the scattering rate is dominated by piezo-acoustic coupling with phonons around 3 meV and by longitudinal-optical (LO) phonons around 89 meV; these modes are shown by blue lines in the phonon dispersion plots of Figure 2I. Moving to $CsPbI_3$ in Figure 3B, we see three distinct peaks contributing to the scattering rate (labeled as 2, 3, and 4), as well as a small background contribution. The three sharp peaks originate from LO modes of $CsPbI_3$, namely, the bending mode at 2.3 meV (peak 3), the A-site displacement mode at 4.6 meV (peak 2), and the Pb−I stretch mode at 15.8 meV (peak 4). The atomic displacements corresponding to these modes are shown in Figure 3G−I. The background is due to acoustic modes and transverse-optical (TO) phonons, but this contribution is much weaker than in GaN, because piezoacoustic scattering in $CsPbI_3$ is forbidden by inversion symmetry. Of the three peaks, the Pb−I stretch mode dominates and accounts for approximately half of the scattering rate. Moving now to $MAPbI_3$ in Figure 3A, we recognize distinct peaks around 4.3 and 14.4 meV (peaks 2 and 4), which are similar to the case of $CsPbI_3$, only much broader. The broadening results from the hybridization of the PbI_3 vibrations with those of the organic cations,[52] although the character of the modes remains essentially unchanged. Around 3 meV we find a weak Pb−I−Pb rocking mode (peak 1), and the A-site displacement mode is now at higher energy, at 10.2 meV (peak 3). We also see a broad structure around 21 meV, which originates from librational modes of MA^+ (peak 5). The characteristic displacement patterns of three of those five modes are shown in Figure 3D−F. Our Boltzmann transport formalism relies on the assumption of harmonic phonons. The use of the harmonic approximation is justified, because the only anharmonic modes in the orthorhombic phase of $MAPbI_3$ are associated with the spinning of the MA cation around the C−N axis with an energy of 16 meV,[53] and as shown in Figure 3A, these modes have a negligible contribution to the scattering rate. Also in the case of $MAPbI_3$ the contribution of acoustic and TO phonons is essentially negligible, and piezoacoustic scattering is inactive.

Using this understanding we can explain why the mobilities in halide perovskites are more than an order of magnitude smaller than in n-type GaN (30−80 $cm^2/(V\ s)$ vs 810 $cm^2/(V\ s)$ at room temperature (Figure 1). Because we established that in $MAPbI_3$ the carrier mobility is dominated by polar-phonon scattering, we can simplify eqs 1 and 2 to focus specifically on the contributions arising from Fröhlich interactions. We already noted that the effective masses of $MAPbI_3$ are similar to the electron effective mass of GaN; therefore, the possible origin of the difference between GaN and $MAPbI_3$ must reside in the scattering rates $1/\tau_{nk}$ in eq 2. A straightforward estimate shows that in GaN there are essentially no LO phonons at room temperature ($n_{q\nu}$= 0.03 for $\hbar\omega_{LO}$= 90 meV and k_BT = 25.7 meV), therefore scattering via LO phonon absorption is extremely weak. On the other hand, electrons within an energy $\hbar\omega_{\mathrm{LO}}$ cannot emit phonons, otherwise the final states would be inside the band gap. Therefore, the electronic states that dominate the scattering integral due to the Fermi factor $\partial f_{n\mathbf{k}}/\partial\varepsilon_{n\mathbf{k}} \propto \exp(-\varepsilon_{n\mathbf{k}}/k_{\mathrm{B}}T)$ in eq 1 are essentially immune to LO-phonon scattering. This effect accounts for the large electron mobilities observed in GaN. These considerations cease to hold in the case of $\mathrm{MAPbI_3}$. In fact we now have LO phonons in the range $\hbar\omega_{\mathrm{LO}}$ = 5−20 meV. As a result, both phonon absorption and emission are allowed, and the corresponding Bose−Einstein factors are large ($n_{\mathbf{q}\nu}$ = 0.8−4.6). The electron scattering rates are correspondingly much higher than in GaN, as seen in Figure 2A,C. Therefore, the large difference in mobility between $\mathrm{MAPbI_3}$ and GaN originates primarily from different phonon energy scales.

In order to place this reasoning on more quantitative grounds, we developed a simplified conceptual model, obtained from eqs 1 and 2 by considering electrons with effective mass m^* interacting with a single LO phonon of energy $\hbar\omega_{\mathrm{LO}}$ via the standard Fröhlich coupling strength α. In the Supporting Information, section 2 we show that, under these approximations, the mobility depends only on two dimensionless parameters, a "polar mass" $\alpha(m^*/m_e)$ and a "reduced frequency" $\hbar\omega_{\mathrm{LO}}/k_{\mathrm{B}}T$. Figure 4 shows a map of the mobility as a function of these parameters. We see that high mobilities can be achieved when the polar mass is small and the phonon frequency is large. The complete analytical expression of the mobility in terms of these parameters is given in the Supporting Information, section 2 (see eqs S6−S9); however, to a first approximation, this trend can be captured by the dimensionless scaling law:

$$\mu/(e\hbar/m_e k_{\mathrm{B}}T) = [0.052(\hbar\omega_{\mathrm{LO}}/k_{\mathrm{B}}T)^{3.3} + 0.34]/(\alpha m^*/m_e) \tag{3}$$

We called this relation a "universal scaling law" to highlight its broad validity across the class of halide perovskites considered here and its dependence on dimensionless scaling parameters. Using this law, a stiffening of the phonon frequencies by a factor of 89/13 $\simeq$ 6.8 (GaN/$\mathrm{MAPbI_3}$) leads to an increase in the room-temperature mobility by a factor of ~9.7. Furthermore, a reduction of the polar mass by 0.34/0.09 $\simeq$ 3.8 (Supporting Information, Table S2) increases the mobility by the same factor. These two effects combined fully explain why the mobility attainable in $\mathrm{MAPbI_3}$ is ~40 times lower than in a classic optoelectronic material like GaN. We can estimate the accuracy of our calculations by noting that our computed reduced effective mass underestimates the experimental value by 6%, and our LO phonon frequency (see Table S3) overestimates the experimental value by 10%.[54] These two effects tend to cancel according to eq 3 and lead to an uncertainty of 6% in the mobility.

Guided by the universal mobility map in Figure 4A, we explored the possibility of tuning mobilities in halide perovskites by anion and cation substitution. Naively one would expect that by using lighter elements we would naturally move toward the right side of the map, thus increasing mobilities. However, when we go from $\mathrm{MAPbI_3}$ to $\mathrm{CsPbBr_3}$ we find that a slight increase in the phonon frequency is countered by a much heavier polar mass, and the net effect is a slight decrease in mobility, in agreement with previous calculations based on the Fröhlich model.[39,40] Unlike this simplified model, direct ab initio calculations predict a slightly larger mobility for $\mathrm{CsPbBr_3}$ than for $\mathrm{MAPbI_3}$ (see Table S3). This trend is in line with recent time-of-flight mobility measurements of $\mathrm{MAPbBr_3}$[57,58] that report a higher mobility than for $\mathrm{MAPbI_3}$. The discrepancy between the single-phonon model of eq 3 and the complete calculation highlights the importance of considering a multiphonon Fröhlich coupling for an accurate description of halide perovskites,[41] as can be seen in Figure 3A,B. In addition, the substitution of Pb by Sn appears to be very promising, as the polar mass decreases substantially, while the reduced frequency remains almost unchanged. These findings indicate that Sn-based halide perovskites or mixed Pb/Sn halide perovskites should be considered as primary targets in the quest for more efficient materials for halide optoelectronics.

As an illustration of the benefits of realizing high-mobility halide perovskites, we show in Figure 4B how two figures of merit for photodetectors and thin-film transistors, the photoconductive gain and the switching frequency, vary across the map of Figure 4A. It is clear that the realization of stable Sn-based perovskites, mixed Pb/Sn perovskites, and their derivatives could lead to an order-of-magnitude increase in these performance metrics over Pb-only compounds, thereby opening entirely new opportunities in solution-processable optoelectronics.

In summary, we developed the first complete nonempirical theory of carrier mobilities in halide perovskites. We demonstrated that the maximum achievable carrier mobilities in these materials are set by the Fröhlich electron−phonon coupling associated with the stretching motion of the Pb−I bonds. By performing a comparative analysis between halide perovskites and standard inorganic semiconductors, we established that the relatively low mobilities observed so far in these materials result from the very low frequency of the Pb−I vibrations, which leads to significant thermal activation of phonons at room temperature. More generally, we identified a universal scaling law that underpins carrier transport in these compounds, and we proposed a mobility map to rationalize the transport properties of all halide perovskites. Our study will serve as a simple conceptual framework to understand the theoretical performance limits of these compounds and to guide the design of new materials and devices for perovskite optoelectronics.

■ ASSOCIATED CONTENT

Ⓢ Supporting Information

The Supporting Information is available free of charge on the ACS Publications website at DOI: 10.1021/acsenergylett.8b02346.

Full description of the materials and methods used in this paper, relying on refs 13, 16, 23, 24, 41, 52, and 59−70; Figures S1−S6; and Tables S1−S4 (PDF)

■ AUTHOR INFORMATION

Corresponding Author

*E-mail: feliciano.giustino@materials.ox.ac.uk.

ORCID

Samuel Poncé: 0000-0003-1159-8389

Martin Schlipf: 0000-0003-3198-0497

Feliciano Giustino: 0000-0001-9293-1176

Notes

The authors declare no competing financial interest.

ACKNOWLEDGMENTS

The research leading to these results has received funding from the Leverhulme Trust (Grant RL-2012-001), the Graphene Flagship Core2 (Grant No. 785219), and the UK EPSRC (Grant No. EP/M020517/1). The authors acknowledge the use of the University of Oxford Advanced Research Computing (ARC) facility (http://dx.doi.org/10.5281/zenodo.22558); the ARCHER UK National Supercomputing Service under the "T-Dops" project, the DECI resource "Cartesius" based in The Netherlands at SURFsara, and "Abel" based in Oslo with support from the PRACE AISBL, PRACE-15, and PRACE-17 for awarding us access to MareNostrum at BSC-CNS, Spain and CSD3, UK EPSRC (Grant EP/P020259/1).

REFERENCES

(1) Green, M. A.; Ho-Baillie, A.; Snaith, H. J. The Emergence of Perovskite Solar Cells. *Nat. Photonics* **2014**, *8*, 506−514.

(2) Stranks, S.; Snaith, H. J. Metal-Halide Perovskites for Photovoltaic and Light-Emitting Devices. *Nat. Nanotechnol.* **2015**, *10*, 391−402.

(3) Kojima, A.; Teshima, K.; Shirai, Y.; Miyasaka, T. Organometal Halide Perovskites as Visible-Light Sensitizers for Photovoltaic Cells. *J. Am. Chem. Soc.* **2009**, *131*, 6050−6051.

(4) Lee, M. M.; Teuscher, J.; Miyasaka, T.; Murakami, T.; Snaith, H. Efficient Hybrid Solar Cells based on Meso-Superstructured Organometal Halide Perovskites. *Science* **2012**, *338*, 643−647.

(5) Kim, H.-S.; Lee, C.-R.; Im, J.-H.; Lee, K.-B.; Moehl, T.; Marchioro, A.; Moon, S.-J.; Humphry-Baker, R.; Yum, J.-H.; Moser, J. E.; et al. Lead Iodide Perovskite Sensitized All-Solid-State Submicron Thin Film Mesoscopic Solar Cell with Efficiency Exceeding 9%. *Sci. Rep.* **2012**, *2*, 591.

(6) Tan, Z.-K.; Moghaddam, R. S.; Lai, M. L.; Docampo, P.; Higler, R.; Deschler, F.; Price, M.; Sadhanala, A.; Pazos, L. M.; Credgington, D.; et al. Bright Light-Emitting Diodes based on Organometal Halide Perovskite. *Nat. Nanotechnol.* **2014**, *9*, 687−692.

(7) Zhu, H.; Fu, Y.; Meng, F.; Wu, X.; Gong, Z.; Ding, Q.; Gustafsson, M. V.; Trinh, M. T.; Jin, S.; Zhu, X.-Y. Lead Halide Perovskite Nanowire Lasers with Low Lasing Thresholds and High Quality Factors. *Nat. Mater.* **2015**, *14*, 636−642.

(8) Ha, S.-T.; Shen, C.; Zhang, J.; Xiong, Q. Laser Cooling of Organic-Inorganic Lead Halide Perovskites. *Nat. Photonics* **2016**, *10*, 115−121.

(9) Shrestha, S.; Fischer, R.; Matt, G. J.; Feldner, P.; Michel, T.; Osvet, A.; Levchuk, I.; Merle, B.; Golkar, S.; Chen, H.; et al. High-performance Direct Conversion X-Ray Detectors based on Sintered Hybrid Lead Triiodide Perovskite Wafers. *Nat. Photonics* **2017**, *11*, 436−440.

(10) Park, S.; Chang, W. J.; Lee, C. W.; Park, S.; Ahn, H.-Y.; Nam, K. T. Photocatalytic Hydrogen Generation from Hydriodic Acid using Methylammonium Lead Iodide in Dynamic Equilibrium with Aqueous Solution. *Nat. Energy* **2017**, *2*, 16185.

(11) García de Arquer, F. P.; Armin, A.; Meredith, P.; Sargent, E. H. Solution-Processed Semiconductors for Next-Generation Photodetectors. *Nat. Rev. Mater.* **2017**, *2*, 16100.

(12) Lin, Y.-H.; Pattanasattayavong, P.; Anthopoulos, T. D. Metal-Halide Perovskite Transistors for Printed Electronics: Challenges and Opportunities. *Adv. Mater.* **2017**, *29*, 1702838.

(13) Senanayak, S. P.; Yang, B.; Thomas, T. H.; Giesbrecht, N.; Huang, W.; Gann, E.; Nair, B.; Goedel, K.; Guha, S.; Moya, X.; et al. Understanding Charge Transport in Lead Iodide Perovskite Thin-Film Field-Effect Transistors. *Sci. Adv.* **2017**, *3*, No. e1601935.

(14) Yablonovitch, E. Lead Halides Join the Top Optoelectronic League. *Science* **2016**, *351*, 1401−1401.

(15) Akinwande, D.; Petrone, N.; Hone, J. Two-dimensional Flexible Nanoelectronics. *Nat. Commun.* **2014**, *5*, 5678.

(16) Davies, C. L.; Filip, M. R.; Patel, J. B.; Crothers, T. W.; Verdi, C.; Wright, A.; Milot, R. L.; Giustino, F.; Johnston, M. B.; Herz, L. M. Bimolecular Recombination in Methylammonium Lead Triiodide Perovskite is an Inverse Absorption Process. *Nat. Commun.* **2018**, *9*, 293.

(17) Herz, L. M. Charge-Carrier Mobilities in Metal Halide Perovskites: Fundamental Mechanisms and Limits. *ACS En. Lett.* **2017**, *2*, 1539−1548.

(18) Saidaminov, M. I.; Abdelhady, A. L.; Murali, B.; Alarousu, E.; Burlakov, V. M.; Peng, W.; Dursun, I.; Wang, L.; He, Y.; Maculan, G.; et al. High-Quality Bulk Hybrid Perovskite Single Crystals within Minutes by Inverse Temperature Crystallization. *Nat. Commun.* **2015**, *6*, 7586.

(19) Motta, C.; El-Mellouhi, F.; Sanvito, S. Charge Carrier Mobility in Hybrid Halide Perovskites. *Sci. Rep.* **2015**, *5*, 12746.

(20) Filippetti, A.; Mattoni, A.; Caddeo, C.; Saba, M. I.; Delugas, P. Low Electron-Polar Optical Phonon Scattering as a Fundamental Aspect of Carrier Mobility in Methylammonium Lead Halide $CH_3NH_3PbI_3$ Perovskites. *Phys. Chem. Chem. Phys.* **2016**, *18*, 15352−15362.

(21) Zhao, T.; Shi, W.; Xi, J.; Wang, D.; Shuai, Z. Intrinsic and Extrinsic Charge Transport in $CH_3NH_3PbI_3$ Perovskites Predicted from First-Principles. *Sci. Rep.* **2016**, *6*, 19968.

(22) Lee, J.-H.; Deng, Z.; Bristowe, N. C.; Bristowe, P. D.; Cheetham, A. K. The Competition between Mechanical Stability and Charge Carrier Mobility in MA-based Hybrid Perovskites: insight from DFT. *J. Mater. Chem. C* **2018**, *6*, 12252−12259.

(23) Poncé, S.; Margine, E. R.; Giustino, F. Towards Predictive Many-Body Calculations of Phonon-Limited Carrier Mobilities in Semiconductors. *Phys. Rev. B: Condens. Matter Mater. Phys.* **2018**, *97*, 121201.

(24) Milot, R. L.; Eperon, G. E.; Snaith, H. J.; Johnston, M. B.; Herz, L. M. Temperature-Dependent Charge-Carrier Dynamics in $CH_3NH_3PbI_3$ Perovskite Thin Films. *Adv. Funct. Mater.* **2015**, *25*, 6218−6227.

(25) Karakus, M.; Jensen, S. A.; D'Angelo, F.; Turchinovich, D.; Bonn, M.; Cánovas, E. Phonon-Electron Scattering Limits Free Charge Mobility in Methylammonium Lead Iodide Perovskites. *J. Phys. Chem. Lett.* **2015**, *6*, 4991−4996.

(26) Shi, D.; Adinolfi, V.; Comin, R.; Yuan, M.; Alarousu, E.; Buin, A.; Chen, Y.; Hoogland, S.; Rothenberger, A.; Katsiev, K.; et al. Low Trap-State Density and Long Carrier Diffusion in Organolead Trihalide Perovskite Single Crystals. *Science* **2015**, *347*, 519−522.

(27) Dong, Q.; Fang, Y.; Shao, Y.; Mulligan, P.; Qiu, J.; Cao, L.; Huang, J. Electron-Hole Diffusion Lengths > 175μm in Solution-Grown $CH_3NH_3PbI_3$ Single Crystals. *Science* **2015**, *347*, 967−970.

(28) Shrestha, S.; Matt, G. J.; Osvet, A.; Niesner, D.; Hock, R.; Brabec, C. J. Assessing Temperature Dependence of Drift Mobility in Methylammonium Lead Iodide Perovskite Single Crystals. *J. Phys. Chem. C* **2018**, *122*, 5935−5939.

(29) Sadhanala, A.; Kumar, A.; Pathak, S.; Rao, A.; Steiner, U.; Greenham, N. C.; Snaith, H. J.; Friend, R. H. Electroluminescence from Organometallic Lead Halide Perovskite-Conjugated Polymer Diodes. *Adv. Electron. Mater.* **2015**, *1*, 1500008.

(30) Richter, J. M.; Abdi-Jalebi, M.; Sadhanala, A.; Tabachnyk, M.; Rivett, J. P.; Pazos-Outón, L. M.; Gödel, K. C.; Price, M.; Deschler, F.; Friend, R. H. Enhancing Photoluminescence Yields in Lead Halide Perovskites by Photon Recycling and Light Out-coupling. *Nat. Commun.* **2016**, *7*, 13941.

(31) Götz, W.; Romano, L. T.; Walker, J.; Johnson, N. M.; Molnar, R. J. Hall-Effect Analysis of GaN Films Grown by Hydride Vapor Phase Epitaxy. *Appl. Phys. Lett.* **1998**, *72*, 1214−1216.

(32) Jacoboni, C.; Canali, C.; Ottaviani, G.; Quaranta, A. A. A Review of Some Charge Transport Properties of Silicon. *Solid-State Electron.* **1977**, *20*, 77−89.

(33) Stoumpos, C. C.; Malliakas, C. D.; Kanatzidis, M. G. Semiconducting Tin and Lead Iodide Perovskites with Organic Cations: Phase Transitions, High Mobilities, and Near-Infrared Photoluminescent Properties. *Inorg. Chem.* **2013**, *52*, 9019−9038.

(34) Franssen, W. M. J.; van Es, S. G. D.; Dervişoğlu, R.; de Wijs, G. A.; Kentgens, A. P. M. Symmetry, Dynamics, and Defects in Methylammonium Lead Halide Perovskites. *J. Phys. Chem. Lett.* **2017**, *8*, 61−66.

(35) Bernard, G. M.; Wasylishen, R. E.; Ratcliffe, C. I.; Terskikh, V.; Wu, Q.; Buriak, J. M.; Hauger, T. Methylammonium Cation Dynamics in Methylammonium Lead Halide Perovskites: A Solid-State NMR Perspective. *J. Phys. Chem. A* **2018**, *122*, 1560−1573.

(36) Weller, M. T.; Weber, O. J.; Henry, P. F.; Di Pumpo, A. M.; Hansen, T. C. Complete Structure and Cation Orientation in the Perovskite Photovoltaic Methylammonium Lead Iodide between 100 and 352 K. *Chem. Commun.* **2015**, *51*, 4180−4183.

(37) Yi, H. T.; Wu, X.; Zhu, X.; Podzorov, V. Intrinsic Charge Transport across Phase Transitions in Hybrid Organo-Inorganic Perovskites. *Adv. Mater.* **2016**, *28*, 6509−6514.

(38) Chen, Y.; Wu, X.; Yi, H. T.; Haroldson, R.; Gartstein, Y. N.; Rodionov, Y. I.; Tikhonov, K. S.; Zakhidov, A.; Zhu, X. Y.; Podzorov, V. Extended Carrier Lifetimes and Diffusion in Hybrid Perovskites revealed by Hall Effect and Photoconductivity Measurements. *Nat. Commun.* **2016**, *7*, 12253.

(39) Sendner, M.; Nayak, P. K.; Egger, D. A.; Beck, S.; Müller, C.; Epding, B.; Kowalsky, W.; Kronik, L.; Snaith, H. J.; Pucci, A.; et al. Optical Phonons in Methylammonium Lead Halide Perovskites and Implications for Charge Transport. *Mater. Horiz.* **2016**, *3*, 613−620.

(40) Frost, J. M. Calculating Polaron Mobility in Halide Perovskites. *Phys. Rev. B: Condens. Matter Mater. Phys.* **2017**, *96*, 195202.

(41) Schlipf, M.; Poncé, S.; Giustino, F. Carrier Lifetimes and Polaronic Mass Enhancement in the Hybrid Halide Perovskite $CH_3NH_3PbI_3$from Multiphonon Fröhlich Coupling. *Phys. Rev. Lett.* **2018**, *121*, 086402.

(42) Giustino, F. Electron-Phonon Interactions from First Principles. *Rev. Mod. Phys.* **2017**, *89*, 015003.

(43) Schultz, T. D. Slow Electrons in Polar Crystals: Self-Energy, Mass, and Mobility. *Phys. Rev.* **1959**, *116*, 526−543.

(44) Ōsaka, Y. Theory of Polaron Mobility. *Prog. Theor. Phys.* **1961**, *25*, 517−536.

(45) Miyata, K.; Meggiolaro, D.; Trinh, M. T.; Joshi, P. P.; Mosconi, E.; Jones, S. C.; De Angelis, F.; Zhu, X.-Y. Large Polarons in Lead Halide Perovskites. *Sci. Adv.* **2017**, *3*, e1701217.

(46) Ambrosio, F.; Wiktor, J.; De Angelis, F.; Pasquarello, A. Origin of Low Electron-Hole Recombination Rate in Metal Halide Perovskites. *Energy Environ. Sci.* **2018**, *11*, 101−105.

(47) Bretschneider, S. A.; Ivanov, I.; Wang, H. I.; Miyata, K.; Zhu, X.; Bonn, M. Quantifying Polaron Formation and Charge Carrier Cooling in Lead-Iodide Perovskites. *Adv. Mater.* **2018**, *30*, 1707312.

(48) Miyata, A.; Mitioglu, A.; Plochocka, P.; Portugall, O.; Wang, J. T.-W.; Stranks, S. D.; Snaith, H.; Nicholas, R. J. Direct Measurement of the Exciton Binding Energy and Effective Masses for Charge Carriers in Organic-Inorganic Tri-Halide Perovskites. *Nat. Phys.* **2015**, *11*, 582.

(49) Saidi, W. A.; Poncé, S.; Monserrat, B. Temperature Dependence of the Energy Levels of Methylammonium Lead Iodide Perovskite from First-Principles. *J. Phys. Chem. Lett.* **2016**, *7*, 5247.

(50) Filip, M. R.; Eperon, G. E.; Snaith, H.; Giustino, F. Steric Engineering of Metal-Halide Perovskites with Tunable Optical Band Gaps. *Nat. Commun.* **2014**, *5*, 5757.

(51) Marronnier, A.; Roma, G.; Boyer-Richard, S.; Pedesseau, L.; Jancu, J.-M.; Bonnassieux, Y.; Katan, C.; Stoumpos, C. C.; Kanatzidis, M. G.; Even, J. Anharmonicity and Disorder in the Black Phases of Cesium Lead Iodide Used for Stable Inorganic Perovskite Solar Cells. *ACS Nano* **2018**, *12*, 3477.

(52) Pérez-Osorio, M. A.; Milot, R. L.; Filip, M. R.; Patel, J. B.; Herz, L. M.; Johnston, M. B.; Giustino, F. Vibrational Properties of the Organic-Inorganic Halide Perovskite $CH_3NH_3PbI_3$ from Theory and Experiment: Factor Group Analysis, First-Principles Calculations, and Low-Temperature Infrared Spectra. *J. Phys. Chem. C* **2015**, *119*, 25703−25718.

(53) Pérez-Osorio, M. A.; Lin, Q.; Phillips, R. T.; Milot, R. L.; Herz, L. M.; Johnston, M. B.; Giustino, F. Raman Spectrum of the Organic−Inorganic Halide Perovskite $CH_3NH_3PbI_3$ from First Principles and High-Resolution Low-Temperature Raman Measurements. *J. Phys. Chem. C* **2018**, *122*, 21703−21717.

(54) Wright, A. D.; Verdi, C.; Milot, R. L.; Eperon, G. E.; Pérez-Osorio, M. A.; Snaith, H. J.; Giustino, F.; Johnston, M. B.; Herz, L. M. Electron-Phonon Coupling in Hybrid Lead Halide Perovskites. *Nat. Commun.* **2016**, *7*, 11755 Article .

(55) Muñoz, E.; Monroy, E.; Garrido, J. A.; Izpura, I.; Sánchez, F. J.; Sánchez-García, M. A.; Calleja, E.; Beaumont, B.; Gibart, P. Photoconductor Gain Mechanisms in GaN Ultraviolet Detectors. *Appl. Phys. Lett.* **1997**, *71*, 870−872.

(56) Santoruvo, G.; Matioli, E. In-Plane-Gate GaN Transistors for High-Power RF Applications. *IEEE Electron Device Lett.* **2017**, *38*, 1413−1416.

(57) Wei, Y.; Fang, H.; Mulligan, P.; Chuirazzi, W.; Fang, H.-H.; Wang, C.; Ecker, B. R.; Gao, Y.; Loi, M. A.; Cao, L.; Huang, J. Sensitive X-ray Detectors made of Methylammonium Lead Tribromide Perovskite Single Crystals. *Nat. Photonics* **2016**, *10*, 333.

(58) Wei, H.; DeSantis, D.; Wei, W.; Deng, Y.; Guo, D.; Savenije, T. J.; Cao, L.; Huang, J. Dopant Compensation in Alloyed $CH_3NH_3PbBr_{3-x}Cl_x$ Perovskite single Crystals for Gamma-Ray Spectroscopy. *Nat. Mater.* **2017**, *16*, 826.

(59) Giannozzi, P.; Andreussi, O.; Brumme, T.; Bunau, O.; Buongiorno Nardelli, M.; Calandra, M.; Car, R.; Cavazzoni, C.; Ceresoli, D.; Cococcioni, M.; et al. Advanced Capabilities for Materials Modelling with Quantum ESPRESSO. *J. Phys.: Condens. Matter* **2017**, *29*, 465901.

(60) Hamann, D. R. Optimized Norm-Conserving Vanderbilt Pseudopotentials. *Phys. Rev. B: Condens. Matter Mater. Phys.* **2013**, *88*, 085117.

(61) van Setten, M.; Giantomassi, M.; Bousquet, E.; Verstraete, M.; Hamann, D.; Gonze, X.; Rignanese, G.-M. The PseudoDojo: Training and Grading a 85 Element Optimized Norm-Conserving Pseudopotential Table. *Comput. Phys. Commun.* **2018**, *226*, 39−54.

(62) Baikie, T.; Fang, Y.; Kadro, J. M.; Schreyer, M.; Wei, F.; Mhaisalkar, S. G.; Graetzel, M.; White, T. J. Synthesis and Crystal Chemistry of the Hybrid Perovskite $(CH_3NH_3)PbI_3$ for Solid-State Sensitised Solar Cell Applications. *J. Mater. Chem. A* **2013**, *1*, 5628−5641.

(63) Vurgaftman, I.; Meyer, J. R.; Ram-Mohan, L. R. Band Parameters for III-V Compound Semiconductors and their Alloys. *J. Appl. Phys.* **2001**, *89*, 5815−5875.

(64) Mingo, N.; Stewart, D. A.; Broido, D. A.; Srivastava, D. Phonon Transmission through Defects in Carbon Nanotubes from First Principles. *Phys. Rev. B: Condens. Matter Mater. Phys.* **2008**, *77*, 033418.

(65) Marini, A.; Hogan, C.; Grüning, M.; Varsano, D. Yambo: An *ab initio* Tool for Excited State Calculations. *Comput. Phys. Commun.* **2009**, *180*, 1392−1403.

(66) Godby, R. W.; Needs, R. J. Metal-Insulator Transition in Kohn-Sham theory and Quasiparticle theory. *Phys. Rev. Lett.* **1989**, *62*, 1169−1172.

(67) Bruneval, F.; Gonze, X. Accurate *GW* Self-Energies in a Plane-Wave Basis Using Only a Few Empty States: Towards Large Systems. *Phys. Rev. B: Condens. Matter Mater. Phys.* **2008**, *78*, 085125.

(68) Poncé, S.; Margine, E. R.; Verdi, C.; Giustino, F. EPW: Electron-Phonon Coupling, Transport and Superconducting Properties using Maximally Localized Wannier Functions. *Comput. Phys. Commun.* **2016**, *209*, 116−133.

(69) Mostofi, A. A.; Yates, J. R.; Pizzi, G.; Lee, Y.-S.; Souza, I.; Vanderbilt, D.; Marzari, N. An updated Version of Wannier90: A Tool for Obtaining Maximally-Localised Wannier Functions. *Comput. Phys. Commun.* **2014**, *185*, 2309−2310.

(70) Chen, H.-W.; Sakai, N.; Jena, A. K.; Sanehira, Y.; Ikegami, M.; Ho, K.-C.; Miyasaka, T. A Switchable High-Sensitivity Photodetecting and Photovoltaic Device with Perovskite Absorber. *J. Phys. Chem. Lett.* **2015**, *6*, 1773−1779.